Development of Nb-GaAs based superconductor-semiconductor hybrid platform by combining *in situ* dc magnetron sputtering and molecular beam epitaxy

Clemens Todt [1,2] Sjoerd Telkamp [1,2] Filip Krizek [1,2,3,4] Christian Reichl,[1,2] Mihai Gabureac,[1,2] Rüdiger Schott [1,2]
Erik Cheah,[1,2] Peng Zeng [5] Thomas Weber [6] Arnold Müller,[7] Christof Vockenhuber,[7]
Mohsen Bahrami Panah,[1,2] and Werner Wegscheider[1,2]

[1]*Solid State Physics Laboratory, ETH Zürich, CH-8093 Zürich, Switzerland*
[2]*Quantum Center, ETH Zürich, CH-8093 Zürich, Switzerland*
[3]*IBM Research Europe - Zurich, 8803 Rüschlikon, Switzerland*
[4]*Institute of Physics, Czech Academy of Sciences, 162 00 Prague, Czech Republic*
[5]*ETH Zürich, The Scientific Center for Optical and Electron Microscopy (ScopeM), CH 8093 Zürich, Switzerland*
[6]*X-ray Platform, Department of Materials, ETH Zürich, Vladimir-Prelog-Weg 5-10, 8093 Zürich, Switzerland*
[7]*Laboratory of Ion Beam Physics, ETH Zurich, Schafmattstrasse 20, CH-8093 Zurich, Switzerland.*

We present Nb thin films deposited *in situ* on GaAs by combining molecular beam epitaxy and magnetron sputtering within an ultrahigh vacuum cluster. Nb films deposited at varying power, and a reference film from a commercial system, are compared. The results show clear variation between the *in situ* and *ex situ* deposition which we relate to differences in magnetron sputtering conditions and chamber geometry. The Nb films have critical temperatures of around 9 K and critical perpendicular magnetic fields of up to $B_{c2} = 1.4$ T at 4.2 K. From STEM images of the GaAs-Nb interface we find the formation of an amorphous interlayer between the GaAs and the Nb for both the *ex situ* and *in situ* deposited material.

I. INTRODUCTION

Superconductor (SC) semiconductor (SE) hybrid (SSH) devices have reemerged [1–3] fueled by the hope of finding anyons in solid state systems and their subsequent application for fault tolerant quantum computing [4–8]. A large spectrum of experiments has been reported including Andreev interaction with Quantum Hall states [9–11], possible Majorana fermions in solid state systems [12,13], and topological superconductivity [14,15].

The achievement of epitaxial growth of thin film Al on III-V SEs [16,17] brought the necessary material improvement that resulted in the vast body of work on SSH in recent years [18–34]. The crucial element of the material synthesis is the *in situ* deposition, enabling an undisturbed SC-SE combination [17].

The superconducting properties of the epitaxial Al films limit the temperature and magnetic field range of Al-based SSH experiments to T_c of around 1.6 K at film thicknesses between 5 nm and 10 nm [19,20,25,27,28]. The reported perpendicular critical fields B_{c2} range from 30mT [21] up to 164 mT [28] at dilution fridge temperatures.

The search for an alternative to Al is the subject of a multitude of recent studies [35–41]. A wide range of elemental superconductors has been deposited onto nanowires including Pb [37,42], In [43], Ta [36], V [44], and Sn [38,42]. Pb appears to be the best alternative so far [37,42] owing to its favourable lattice match to InAs [45] and relatively high Tc [37]. Nb is of particular interest [35,36,40] as it has the highest bulk critical temperature and magnetic field of all the elemental SCs [46].

Nanowires and two dimensional electron systems (2DES) based on InAs and InSb with an epitaxial Al layer have become the established material platform. Exciting research proposals [47–49] call for building increasingly complex SSH devices and networks. In this application lithographically patterned 2DES-SC SSH represent a promising approach [50].

The primary advantage of GaAs 2DES is that they reach far higher mobilities [51] than 2DES based on InAs [32] and InSb [52]. The drawback of GaAs is the $\Phi_B = 0.77$ eV [53] Schottky barrier which is expected to suppress the proximity effect [54]. Nonetheless, induced superconducting gaps in bulk n-GaAs employing *in situ* deposited Al have been measured [55,56]. In this context our recently developed shallow GaAs 2DESs [51] are posing an interesting unexplored potential for SSHs.

2DES based on GaAs in combination with Nb are suited for vortex mediated interaction between the SC and 2DES. A type-II superconductor can shape the magnetic field in the SE underneath via its vortices [57] forming the basis of exciting experimental proposals [58–60]. Geim *et al.* [61] investigated Pb on a GaAs 2DES and concluded that a small vortex is needed together with a low electron density shallow 2DES. The small vortex size can be achieved in Nb, and GaAs based 2DES reach far lower densities [51] than InAs [62] and InSb [63].

We attempt to extend the range of available material combinations to include GaAs and Nb, with the possible applications in shallow inverted 2DES [51] and in vortex mediated interactions [58]. In this work, we present the first results from our chamber for DC magnetron sputtering of SC on our MBE grown III-V SEs without breaking the vacuum.

In the initial experiment, we compare Nb deposited *in situ* at varying power in the UHV dc magnetron sputtering system and *ex situ* deposited in a commercial system (AJA International). The samples are of high purity but display significant differences in surface roughness and crystallite orientation which can be related to the growth regime.

We compare the superconducting properties of the Nb film, by investigating the resistive transition as a function of temperature and magnetic field. STEM images of the Nb-GaAs interface reveal an amorphous interlayer at the interface for both the *in situ* and *ex situ* depositions.

II. MBE AND MAGNETRON SPUTTERING CLUSTER

The layout of the UHV cluster, consisting of two molecular beam epitaxy (MBE) machines and the SC deposition system, is presented in Fig. 1(a). The first MBE chamber is optimized for high mobility 2DES in (Al)GaAs [51,64–67] while the other covers a wider range of III-V materials based on As and Sb [52,63,68–71]. The UHV magnetron sputtering chamber is connected via a UHV tunnel to enable *in situ* deposition of SCs on MBE grown SEs as well as preventing contamination of the MBE systems.

The incorporation of oxygen in superconducting films is generally believed to have a detrimental effect on the superconducting properties such as the critical temperature [72]. Therefore, the system was designed to minimize contaminants, specifically the incorporation of oxygen. The UHV magnetron sputtering chamber is supplied with purified gas and solely pumped by a cryo pump in order to obtain elementally clean films, see the Supplemental Material for details [73]. After bakeout, the system achieved the mass spectra presented at the bottom Fig. 1(b). The black line represents the pumped state at $p < 1 \times 10^{-10}$ mbar while the red line at $p = 1 \times 10^{-9}$ mbar was taken 18 hrs after the deposition of Nb. The pressure is dominated by peaks from the different ionization states of Ar and its isotopes [36,38]. A peak associated with water three orders of magnitude smaller than Argon can be identified after deposition indicated by the arrow. Continued use of the chamber reduced the water peak below detection limit and therefore we assume that it originated from residual water in the gas lines.

The kinetic rather than thermal nature of magnetron sputtering offers an alternative path to the evaporation for SC deposition on SEs. The film growth via evaporation is primarily controlled by substrate temperature and rate [74]. In order to produce connected films of low melting point elements such as In, Pb, or even Al on SE surfaces, the substrate has to be typically cooled below room temperature [17,37,75,76], adding technical complexity. SC with higher melting points such as Ta and Nb can be grown at higher substrate temperatures [40]. However, to evaporate these low vapor pressure metals [77] they have to be heated to high temperatures causing the chamber to release contamination from the chamber walls and heat up the substrate surface. Magnetron sputtering, on the other hand, is a comparatively cold deposition method [78].

The method appeals additionally with the possibility to grow nitrides, a simple material exchange, wide variety of compounds from mixed targets and co-sputtering, as well
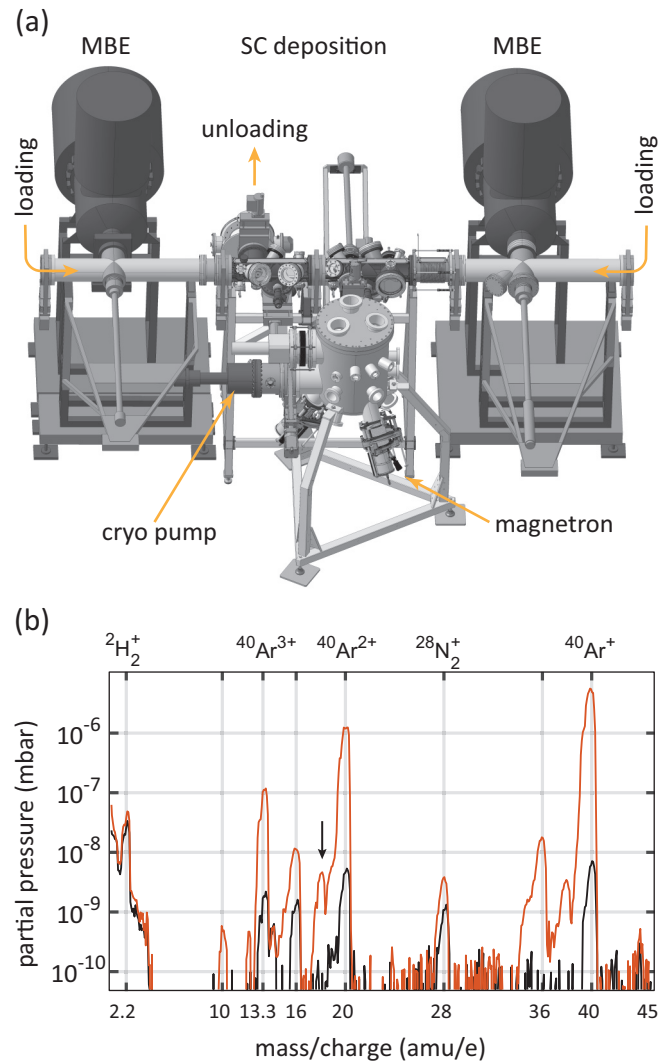

FIG. 1. (a) Layout of the UHV cluster, consisting of two MBE chambers used for semiconductor growth and the magnetron sputtering chamber for superconductor deposition. (b) Mass spectrum of the superconductor deposition chamber. The red line indicates a measurement 18 hrs after a Nb deposition while the black line is a measurement taken after pumping the system for a week. The arrow indicates the minute water peak that appears after deposition.

as a moderate pressure during deposition which limits outgassing [78]. This opens up the possibility to deposit a wide range of compound materials such as A15 and B1 phase SCs, as well as more exotic variants like MgB_2 [79].

A. Sample preparation

Both the *ex situ* and *in situ* Nb films were deposited onto 720 nm of MBE grown n^{++} GaAs. The *ex situ* wafer was removed from the MBE chamber after growth. Before loading it into the AJA magnetron sputtering system the wafer was etched in a 1:1 solution of HCl (32%):H_2O at room temperature until the surface was hydrophilic to remove the oxide. The wafer was then transferred in air to the load lock within 5 min. The *in situ* wafer was moved in our UHV tunnel from the MBE chamber to the UHV magnetron sputtering chamber
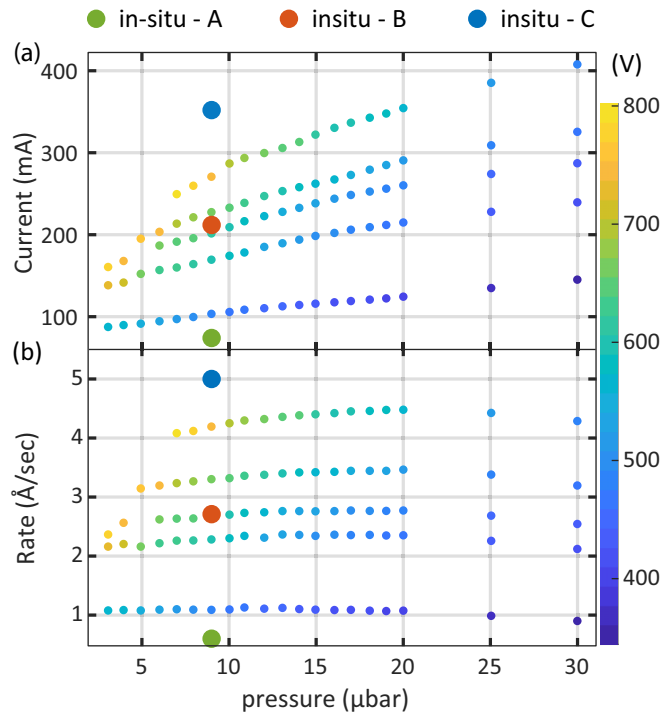
FIG. 2. (a) Current and (b) Nb deposition rate dependence on pressure. The voltage is indicated by the color of the dot and the scale bar. The working conditions for the presented *in situ* films are indicated by the larger dots.

under a residual pressure of $<5 \times 10^{-9}$ mbar. Immediately after the MBE growth run has ended, the structure is cooled rapidly in an As atmosphere for ca. five minutes, until the wafer has reached a temperature $< 500\,°C$. Then the As supply is turned off and the wafers cool to room temperature.

B. Nb depositions

In order to investigate the possible operating conditions in our sputtering system, a characterization of the Nb sputtering rate for various power and pressure combinations was made. This exploration served as a starting point to determine which sputtering conditions could be compared to the commercial AJA system and could yield films with good superconducting parameters.

The dependence of the Nb deposition rate on pressure and set power for our system was investigated using a quartz

crystal balance that can be moved into the wafer position; results are presented in Fig. 2. The rate increases with pressure up to 20 µbar at which point the Nb growth is limited by diffusion from the Ar gas. With increasing pressure the voltage decreases and the current increases, as expected from a denser and more conductive plasma. The rate is linearly dependent on the set power at a given pressure.

The deposition in our system with two inch UHV magnetrons from Angstrom Sciences is controlled by pressure, power, and substrate heating. The parameters used in this study are summarized in Table I. The guns are mounted such that we can vary the substrate target distance under a fixed angle of $32°$ and the substrate is not rotated. For this study we chose to fix the distance at the minimum of 110 mm. The commercial system employs a four inch target 100 mm away from the substrate in a planar orientation and a constant substrate rotation. The pressure was chosen such that the pressure-distance product is 1 µbar for both setups.

Due to the difference in target size between the systems, it is not possible to attain the same rate at the same current and voltage values for both setups. The *ex situ* system can attain a low voltage of 214 V at a high rate while the *in situ* machine is limited to 404 V before the plasma becomes unstable at 9 µbar.

III. STRUCTURAL AND ELEMENTAL ANALYSIS

A. AFM

Figure 3 shows the surface morphologies of the Nb films measured by AFM. All samples have randomly distributed elongated grains, roughly 100 nm long and 20 nm wide. The elongated grains are not oriented with respect to the substrate or the source. Since randomly oriented elongated Niobium grains are also observed on a silicon substrate by Imamura *et al.* [81], a direct relationship between this effect and the GaAs substrate seems unlikely.

The root mean square roughness values obtained from the AFM data using Gwyddion [82] are listed in the last column of Table I. The *in situ* films are distinctively rougher than the *ex situ* film with little difference between the *in situ* films.

B. XRD

XRD measurements were performed with a PANalytical X'PERT PRO MPD diffractometer in Bragg-Brentano reflection geometry and Cu Kα_1 radiation. The measurements of

TABLE I. Comparison of dc sputtering parameters p-pressure, T_{sub}-substrate temperature, voltage, J-current density, and rate with the resulting root mean square roughness R_{sq} obtained from AFM measurements in Fig. 3. The bottom three lines are comparable films from literature, see text.

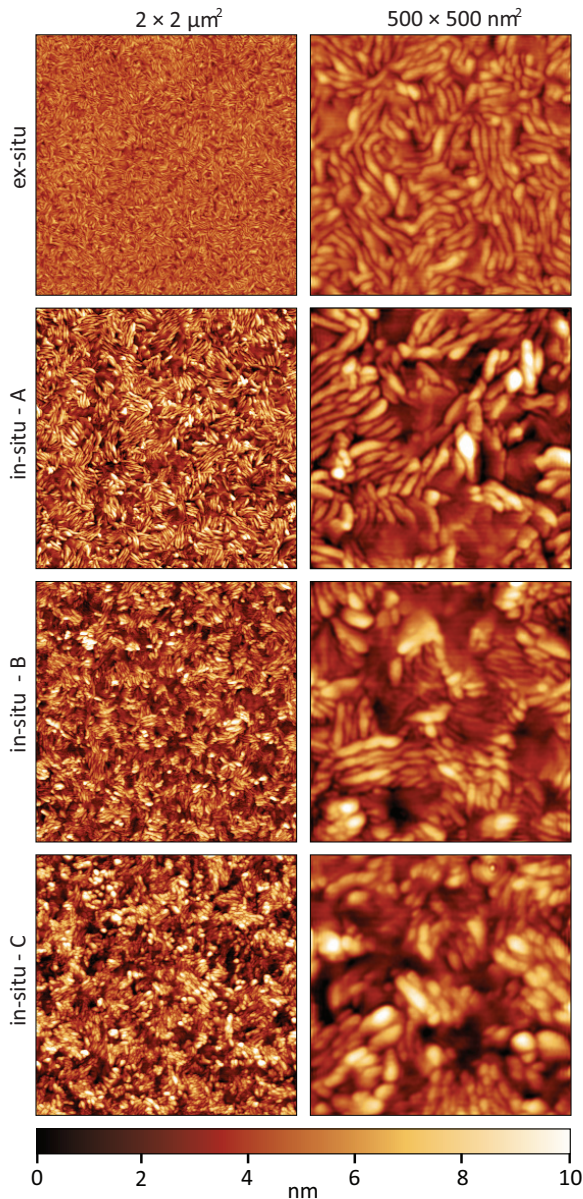| Sample	Substrate	p (µbar)	T_{sub} (°C)	Voltage (V)	J (mA cm^{-2})	Rate (Ås^{-1})	R_{sq} (nm)
Ex situ	GaAs	10	RT	214	24.2	5.0	0.95
In situ A	GaAs	9	RT	404	3.7	0.6	1.84
In situ B	GaAs	9	RT	582	10.6	2.7	1.75
In situ C	GaAs	9	RT	708	17.4	5.0	2.03
[80] B2	Al$_2$O$_3$	4	850	312	2.5	5.0	0.7
[81]	Si	23	RT	270	74	27.3	

FIG. 3. Topography maps of the surface of the *in situ* deposited Nb films A, B, and C and the *ex situ* deposited Nb films. Maps acquired $2 \times 2 \, \mu m^2$ areas are shown in the left panel and from $500 \times 500 \, nm^2$ areas in the right panels.

FIG. 4. XRD measurements using a PANalytical X'PERT PRO MPD diffractometer in Bragg-Brentano reflection geometry and Cu Kα_1 radiation. Tails of the GaAs 001 reflection appear as broad background at $66.1°$ while the sharp contributions at this position are from small slightly misoriented substrate crystallites, likely from the cut edge. (a) is the *ex situ* sample while (b) shows traces from the *in situ* samples vertically offset for clarity.

the Nb films are plotted in Fig. 4. The data was acquired under a two offset of the sample tilt relative to the symmetric geometry to strongly reduce the signal from the single-crystal GaAs substrate relative to the polycrystalline film. Unlike single crystals, the scattering intensity of polycrystalline material is much less sensitive to small rotations of the sample. The signal from the (001) oriented GaAs substrate still appears as broad background centered at $66.1°$, which is coming from thermal diffuse scattering. Apart from the substrate signals, no significant differences are observed between the measurements with and without offset.

Comparison of our XRD data with literature [83,84] shows that our *in situ* Nb films are missing the reflections associated with the (211) orientation parallel to the substrate
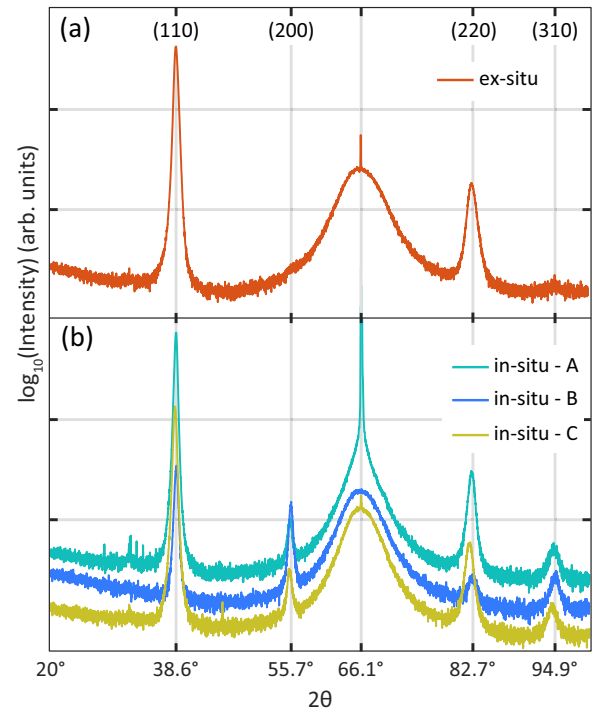
surface [83,84]. The *ex situ* film, on the other hand, only shows the 110 and 220 reflections indicating that the crystallites, making up the uniform film, have a preferential orientation of the (110) planes with respect to the substrate.

The relative peak heights of the 110 family of reflections and the 200 reflection vary between the *in situ* samples while the 310 signal appears unchanged. Depending on deposition voltage and the orientation distribution either the (110) or (200) oriented crystallites appears to vary. However, it is not a direct trend as the largest variation is observed for the *in situ* B sample.

C. Elemental analysis

Rutherford Back Scattering (RBS) measurements of the Nb films were undertaken. The RBS was performed using 2 MeV Helium ions under a back-scattering angle of $167.5°$. The particle induced x-ray emission (PIXE) from the sample was measured in parallel. No significant contamination of the Nb film could be conclusively detected within the capabilities of RBS and PIXE, see the Supplemental Material for details [73].

D. Discussion

The possible origin of the observed structural variations between the *in situ* and *ex situ* films could be related to different deposition parameters, namely voltage, substrate

surface, and/or geometric differences between the two sputtering systems.

It appears, that the large kinetic energy difference related to different powers used for the *in situ* samples do not make a significant difference in their structure that could be identified with the implemented characterization methods. A step up in deposition voltage between the *in situ* and *ex situ* samples does exist. However, we observed very little structural change when changing the voltage from 404 V to 708 V for samples *in situ*—A, B, and C. Given that both systems work at the same pressure distance product, this does not point to the deposition voltage as the root cause for our observed structural differences.

To aid in understanding our findings and bring our deposition conditions into context with those from published literature which have been appended to Table I.

Dobrovolskiy *et al.* [80] have reached the Stranski-Krastanov growth regime [78] and produced epitaxial Nb films at 850 °C on Al_2O_3. The key differences between the reference film by Doborvolskiy *et al.* and our material is the Al_2O_3 substrate which not only has a favourable lattice match but also allows for the required high substrate temperature. The high quality clean limit film listed in Table I has been grown at the same rate as our *ex situ* and *in situ* C samples. In terms of voltage current conditions the reference film is comparable to our *in situ* A sample which suggests that the authors had a smaller substrate target distance to achieve a ten fold higher rate at roughly half the pressure. The roughness increased with elevated growth rate corresponding to a larger voltage which could either be due to the kinetic energy of arriving species or adatoms that didn't have enough time to reach a kink site.

Imamura *et al.* [81] report similarly elongated grains on their Nb films deposited on Si at room temperature. The distance pressure product employed by Imamura *et al.* is close to ours at 1.3 μbar m which could explain the close resemblance. The authors find that with reducing pressure or equivalently increasing voltage, the width of the XRD peaks reduces (therefore crystallite size increases) and the surface becomes smoother. Specifically, the strain went from tensile to compressive at 270 V which corresponds to the point at which crystallite size and roughness did not change anymore. Our *in situ* samples deposited at voltages >404 V appeared to follow this in that roughness and crystallite size did not change.

The random crystallite orientation seen in the XRD in Fig. 4 on the *in situ* material suggests that the Nb does not find a preferential orientation with the substrate. The *in situ* material presents the clean GaAs surface reconstruction while the *ex situ* material was exposed to air. It is therefore less likely that the XRD findings are not originating from the Nb-GaAs interface.

The film growth as we understand it has been discussed in detail by Monti *et al.* [85]. Randomly nucleated crystallites grow in the direction of the facet that incorporates new material at the highest rate. Which facets grow is determined by the surface energy of the specific facet, the adatom mobility on the surface, the direction, and rate of the arriving Nb. This will result in the crystallites with favorable orientation to outgrow and terminate neighboring crystallites until only dendrites of one orientation remain.
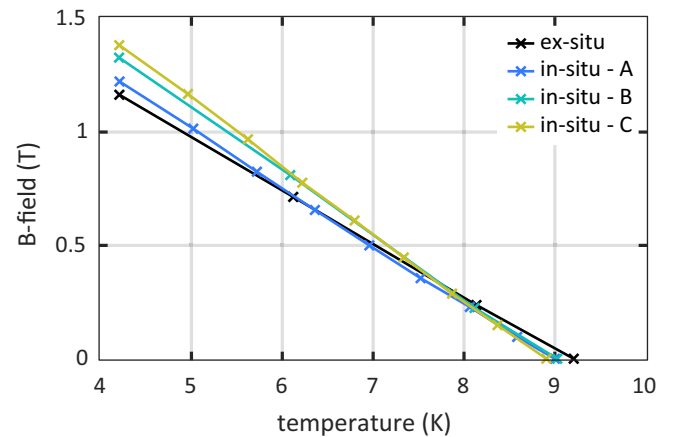

FIG. 5. The resistive superconducting transition as a function of temperature and perpendicular magnetic field for the material deposited *ex situ* and the films A, B, and C deposited *in situ* at a rate of 0.6, 2.7, and 5 Å s^{-1}, respectively.

The fact that the *ex situ* sample only shows the (110) family of crystal orientations parallel to the substrate surface could therefore originate from a fast saturation of the termination process. The (110) facets thus grow the fastest and terminate their neighbours faster in the *ex situ* system than in the *in situ* system. The *in situ* samples on the other hand have not reached the point at which slower growing crystallites are buried resulting in a rougher surface and more crystallite orientations appearing in the XRD. The (211) oriented crystallites have been buried early on in both systems and do not appear at all in the XRD data.

IV. Nb SUPERCONDUCTING PROPERTIES

The critical temperature T_c and critical magnetic field B_{c2} of the Nb films limit the measurement range of SSH devices. B_{c2} is the field applied perpendicular to the film at which the resistive transition occurs, termed the upper critical field associated with type-II superconductors [86]. Knowledge of the resistive superconducting transition can additionally be used to estimate the coherence length of the Cooper pairs. When compared to the mean free path of the electrons ℓ, the coherence length determines whether the superconducting film is in the clean or dirty limit [87].

In the context of proximity induced superconductivity the coherence length appears in the pair breaking parameter indicating that a larger coherence length enhances the pair breaking within the superconductor toward the interface [88].

Van der Pauw structures were made and measured using standard lock-in techniques to determine the sheet resistance as a function of temperature and magnetic field $R(T, B)$, see the Supplemental Material for details [73]. The result of measuring the resistive transitions at a constant temperature, while sweeping the magnetic field, is given in Fig. 5.

The extracted $B_{c2}(T)$ values are significantly higher than expected for clean limit films which have $B_{c2}(0)$ values of 1 T or less [80,89]. It has been reported that dirty limit films have increased critical fields [80,89] while the critical temperature is lower. The large critical field of our films indicates that these

TABLE II. Superconducting properties of the Nb films. The film thicknesses are 100 nm from QCM rates with the exception of *in situ* B which is 90 nm. The reference film by Dobrovolskiy *et al.* [80] is 52 nm thick. The normal state resistivity ρ was measured at 10 K just above the critical temperature T_c. ℓ is the mean free path determined using ρ in Eq. (2). $\xi_{GL}(0)$ is obtained when using the GL Eq. (4). The critical perpendicular magnetic field at zero temperature $B_{c2}(0)$ is estimated from the WHH expression in Eq. (5). The mean free path ℓ in the last column arrived at from the GL the expression in Eq. (8).

Sample	T_c (K)	ρ ($\mu\Omega$cm)	ℓ Eq. (2) (nm)	$B_{c2}(0)$ (T)	$\xi_{GL}(0)$ (nm)	ℓ Eq. (8) (nm)
Ex situ	9.2	47.8	0.8	1.48	15	2.3
In situ A	9.0	32.7	1.1	1.59	14	2.1
In situ B	9.0	43.8	0.8	1.73	14	1.9
In situ C	8.9	71.7	0.5	1.83	13	1.8
[80] B2	9.1	0.45	83	0.7	22	

are in the dirty limit with the *ex situ* sample being closest to the clean limit. The results shown in Fig. 5 indicate that, even for room temperature Nb depositions, it is possible to obtain films with less structural defects by changing the sputtering parameters, such as power and voltage.

The target film thickness was chosen to be 100 nm such that the superconducting critical temperature [90] and critical field [91] of Nb are not expected to significantly change with variations in thickness [92,93]. The thicknesses are determined from QCM deposition rates and time with the *in situ* B sample being slightly thinner at 90 nm.

A. Mean free path

Estimating ℓ from the Drude formula [94]

$$\rho\ell = \frac{m^*}{e^2}\frac{v_F}{n} \tag{1}$$

requires knowledge of the normal state resistivity ρ, the carrier density n, and the effective mass m^* at a temperature just above the superconducting transition. Ideally, each of these parameters is determined from a separate measurement. However, it is common [80,95,96] for Nb films to estimate ℓ just from ρ using the expression by Mayadas *et al.* [97], given as

$$\rho\ell = 3.72 \times 10^{-6} \ \mu\Omega\text{cm}^2 . \tag{2}$$

The normal state resistivity of the sample is calculated from the measured resistance at 10 K and zero applied magnetic field using [98]

$$\rho = \frac{\pi t}{\ln(2)} R(10\,\text{K}, 0\,\text{T}), \tag{3}$$

where t is the Nb film thickness determined from the QCM rate and deposition time. The extracted ℓ values do compare well with published values [80,93,95,99,100] and are listed in the fourth column of Table II.

B. Ginzburg Landau coherence length

The Ginzburg-Landau (GL) coherence length $\xi_{GL}(T)$, which denotes the characteristic length scale over which the order parameter varies, is arrived at via the upper critical field:

$$B_{c2}(T) = \frac{\phi_o}{2\pi\xi_{GL}^2(T)}, \tag{4}$$

where $\phi_o = \frac{h}{2e}$ is the magnetic flux quantum in type-II superconductors.

To obtain a value for $\xi_{GL}(0)$ the zero temperature critical field has to be estimated. The resistive transition $R(T, B)$ from Fig. 5 is not linear down to zero temperature and cannot be simply extrapolated. Werthamer, Helfand, and Hohenberg (WHH) [101] arrived at a relevant theory taking into account no-magnetic impurities, spin paramagnetism, and spin-orbit scattering at high fields based on initial results by Maki [102]. The relevant result from WHH has been presented by Gurevich *et al.* [103] as

$$B_{c2}(0) = 0.69 T_c \left. \frac{dB_{c2}}{dT} \right|_{T=T_c} . \tag{5}$$

Applying this theory produces the values for $B_{c2}(0)$ and $\xi_{GL}(0)$ presented in Table II. The GL coherence length compares well with previously reported values [80,104,105], and the expected $B_{c2}(0)$ are one order of magnitude larger than what has been achieved with thin Al films [28].

C. Bardeen Cooper Schrieffer coherence length

Although Eq. (2) is an established method, there are critiques relevant in the context of thin polycrystalline films [106–108]. It therefore is warranted to sanity check the consistency of Eq. (2) with the Ginzburg-Landau-Abrikosov-Gor'kov (GLAG) theory [109]. It connects the findings of GL and Bardeen-Copper-Schrieffer(BCS) for dirty limit films giving a relation between $\xi_{GL}(T)$ and ξ_o [87] near T_c as

$$\xi_{GL}(T) = 0.85\sqrt{\ell\xi_o}\left(1 - \frac{T}{T_c}\right)^{-\frac{1}{2}}, \tag{6}$$

where ξ_o is the BCS coherence length at zero temperature.

The BCS theory defines the ξ_o as the average distance between the two electrons making up a Cooper pair determined by the uncertainty principle [109]. It reads

$$\xi_o = \frac{\hbar v_F}{\pi \Delta(0)}, \tag{7}$$

where $\Delta(0) = 1.764 k_B T_c$ is the zero temperature BCS gap and v_F the Fermi velocity. Mayadas *et al.* [97] arrive at $v_F = 0.62 \times 10^8$ cm s^{-1} in their derivation of Eq. (2). Using this value we obtain ξ_o between 93 nm for the *ex situ* film and 96 nm for the *in situ* C film.

Combing Eqs. (4) and (6) produces

$$B_{c2}(T) = \frac{\phi_o}{2\pi}\frac{1}{0.7225\ell\xi_o}\frac{T_c - T}{T_c} \tag{8}$$

which expresses the upper critical field to be a linear function of temperature near T_c.

Our data in Fig. 5 is indeed linear which allows us to extract the ℓ from Eq. (8) with ξ_o given by Eq. (7). The resulting

mean free paths are listed in the last column of Table II. The values are close to the results from Eq. (2) listed in Table II and follow the same trend.

D. Discussion

Despite the observed structural changes, the critical temperatures of our Nb films vary only by a few 100 mK. The T_c of the epitaxial clean limit film from Dobrovolskiy *et al.* listed for comparison in Table I falls within the range of our results.

The resistivities of the *in situ* samples increase going down the table correlating with the deposition voltage from Table I. The upper critical field increases significantly going down the table for all samples. Higher resistivities indicate structural degradation which in turn presents more pinning sites for vortices increasing the critical field [110,111]. A significant structural change in AFM and XRD data has only been observed between the *ex situ* and *in situ* samples but not between *in situ* samples. Thus, the electrical measurements appear to be more sensitive to structural changes than the AFM and XRD analysis.

Although the *ex situ* material is smoother and has a preferred crystallite orientation perpendicular to the surface, it does not have the lowest resistivity but a lower critical field and higher critical temperatures. The superconducting properties, AFM, and XRD data all indicate a more homogeneous film which should result in a lower resistivity as exemplified by the reference film by Dobrovolskiy *et al.* listed in Table II. An explanation could be that the *ex situ* film is thinner than we expect.

The resistivity of the clean limit reference film from Dobrovolskiy *et al.* is two orders of magnitude smaller despite the film being half as thick. The additional effect of surface scattering to the resistivities of thin films [106,107] does not appear to be significant down to the 52 nm thickness of the reference film. The large resistivities in our dirty limit films therefore do originate in the structural differences.

The mean free path listed in Table II compared to the extracted coherence lengths confirms that our films are in the dirty limit. The critical field of the clean limit reference film in Table II is 0.7 T. Reducing the power and hence, the voltage, for our *in situ* depositions brings us closer to the clean limit. However, at the given pressure distance of 1 μbar m, we are limited to the results from *in situ* A as the lowest power that results in a stable plasma.

V. Nb-GaAs INTERFACE

ADF STEM images presented in Fig. 6 were taken of the Nb-GaAs interface before and after annealing at 380 °C for 40 s. which is the annealing recipe for ohmic AuGeNi contacts to n^{++} GaAs [112]. An amorphous interlayer can be seen for both the *in situ* B and *ex situ* samples. The thicknesses of the amorphous interlayer indicated in the images were determined by comparing the normalized brightness, see the Supplemental Material for details [73]. The *ex situ* amorphous interface, initially being thicker than in the *in situ* one, is unaffected by the heat, while the *in situ* material shows an increased thickness after tempering.
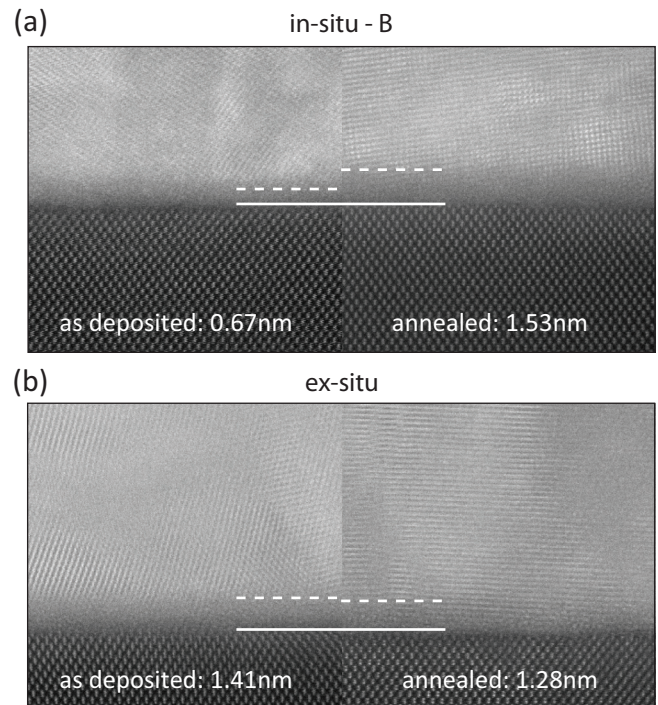

FIG. 6. ADF STEM of the annealed and as deposited *in situ* (a) and *ex situ* (b) Nb-GaAs interface. See the Supplemental Material for complete images and discussion of how the interface widths were determined [73].

The amorphous interface thickness does not increase when annealed for the *ex situ* sample while for the *in situ* it does by 1 nm. The Nb-GaAs interface is expected to be sharp, up to 600 °C for *ex situ* deposited films [113]. However, the quality of the TEM images presented by Ding *et al.* [113] appear to be the limiting factor in the comparison and the interlayer cannot be resolved. Nb deposition on clean GaAs surfaces via magnetron sputtering has been reported [114,115] but is lacking structural investigation of the interface.

The best reference for *in situ* Nb are evaporated films on InAs nanowires, which similarly show an amorphous interlayer [35,36,40]. The origin of the interlayer is attributed to the formation of a Nb_xAs_y compound, which would explain our findings. A cause for the formation of the Nb_xAs_y interface layer might be excess arsenic accumulated on the surface prior to the deposition of Nb.

VI. CONCLUSION

We have investigated both the structural and superconducting properties of Nb films *in situ* deposited on GaAs in a newly designed magnetron sputtering chamber connected to a UHV MBE cluster. An exceptionally high purity of the material was achieved by designing a UHV compatible gas supply system, as proven by the residual gas analysis of the chamber and elemental analysis of the resulting Nb films.

The structural analysis via AFM of the Nb films revealed a marked difference in surface roughness between our *in situ* samples and a reference *ex situ* sample, deposited in a commercial system. Varying the deposition power for the *in situ* samples had little effect on the surface. XRD measurements

further support that difference, with the *ex situ* sample having only the (110) crystallite orientation with respect to the substrate surface. The *in situ* samples all showed (110), (200), and (310) oriented crystallites, despite significant differences in deposition voltages. This difference in crystallinity is attributed to the nucleation and growth of individual crystallites in the polycrystalline film.

Measuring the superconducting resistive transition showed that the films are in the dirty limit with excellent T_c and $B_{c2}(0)$ values. The T_c values did not vary significantly despite a steady increase of $B_{c2}(0)$ with deposition voltage associated with structural degradation. The *in situ* method produces pure films underpinned by RBS and PIXE measurements.

The $B_{c2}(0)$ values reflected subtle structural differences between the *in situ* films. With increasing deposition voltage the critical field increased, indicating that an increased power does have an effect, although we did not resolve a trend in film structure by AFM or XRD.

All the investigated Nb-GaAs interfaces exhibited an amorphous interface layer. Tempering the samples to $380\,^{\circ}$C widens the amorphous layer for the *in situ* B but not the *ex situ* sample. It is unclear if the formation of the amorphous alloy between the materials is purely chemically driven or if it is related to the sputtering process. Interestingly, its presence in the *in situ* deposited samples shows that it is not related to the formation of the native oxide on the semiconductor. Similar phenomena were reported in literature, and the findings indicate that it is related to formation of Nb$_x$As$_y$ alloy [35,36,40].

The presented results validate *in situ* magnetron sputtering as a new path to combine Nb and GaAs. Work is ongoing to employ a wider range of III-V semiconductors and superconductors to built a wider material platform for SSH.

[1] H. Takayanagi and T. Kawakami, Superconducting Proximity Effect in the Native Inversion Layer on InAs, Phys. Rev. Lett. **54**, 2449 (1985).

[2] S. J. Bending, K. von Klitzing, and K. Ploog, Two-dimensional electron gas as a flux detector for a type-II superconducting film, Phys. Rev. B **42**, 9859 (1990).

[3] C. Nguyen, H. Kroemer, and E. L. Hu, Anomalous Andreev Conductance in InAs-AlSb Quantum Well Structures with Nb Electrodes, Phys. Rev. Lett. **69**, 2847 (1992).

[4] A.Yu. Kitaev, Fault-tolerant quantum computation by anyons, Ann. Phys. **303**, 2 (2003).

[5] C. Nayak, S. H. Simon, A. Stern, M. Freedman, and S. Das Sarma, Non-Abelian anyons and topological quantum computation, Rev. Mod. Phys. **80**, 1083 (2008).

[6] J. Alicea, Y. Oreg, G. Refael, F. von Oppen, and M. P. A. Fisher, Non-Abelian statistics and topological quantum information processing in 1D wire networks, Nat. Phys. **7**, 412 (2011).

[7] T. Karzig, C. Knapp, R. M. Lutchyn, P. Bonderson, M. B. Hastings, C. Nayak, J. Alicea, K. Flensberg, S. Plugge, Y. Oreg, C. M. Marcus, and M. H. Freedman, Scalable designs for quasiparticle-poisoning-protected topological quantum computation with Majorana zero modes, Phys. Rev. B **95**, 235305 (2017).

[8] R. Aguado, A perspective on semiconductor-based superconducting qubits, Appl. Phys. Lett. **117**, 240501 (2020).

[9] Z. Wan, A. Kazakov, M. J. Manfra, L. N. Pfeiffer, K. W. West, and L. P. Rokhinson, Induced superconductivity in high-mobility two-dimensional electron gas in gallium arsenide heterostructures, Nat. Commun. **6**, 7426 (2015).

[10] G.-H. Lee, K.-F. Huang, D. K. Efetov, D. S. Wei, S. Hart, T. Taniguchi, K. Watanabe, A. Yacoby, and P. Kim, Inducing superconducting correlation in quantum Hall edge states, Nat. Phys. **13**, 693 (2017).

[11] Ö. Gül, Y. Ronen, S. Y. Lee, H. Shapourian, J. Zauberman, Y. H. Lee, K. Watanabe, T. Taniguchi, A. Vishwanath, A. Yacoby, and P. Kim, Andreev Reflection in the Fractional Quantum Hall State, Phys. Rev. X **12**, 021057 (2022).

[12] A. Das, Y. Ronen, Y. Most, Y. Oreg, M. Heiblum, and H. Shtrikman, Zero-bias peaks and splitting in an Al–InAs nanowire topological superconductor as a signature of Majorana fermions, Nat. Phys. **8**, 887 (2012).

[13] V. Mourik, K. Zuo, S. M. Frolov, S. R. Plissard, E. P. A. M. Bakkers, and L. P. Kouwenhoven, Signatures of majorana fermions in hybrid superconductor-semiconductor nanowire devices, Science **336**, 1003 (2012).

[14] M. Sato and Y. Ando, Topological superconductors: A review, Rep. Prog. Phys. **80**, 076501 (2017).

[15] A. Fornieri, A. M. Whiticar, F. Setiawan, E. Portolés, A. C. C. Drachmann, A. Keselman, S. Gronin, C. Thomas, T. Wang, R. Kallaher, G. C. Gardner, E. Berg, M. J. Manfra, A. Stern, C. M. Marcus, and F. Nichele, Evidence of topological superconductivity in planar Josephson junctions, Nature (London) **569**, 89 (2019).

[16] S. Pilkington and M. Missous, The growth of epitaxial aluminium on As containing compound semiconductors, J. Cryst. Growth **196**, 1 (1999).

[17] P. Krogstrup, N. L. B. Ziino, W. Chang, S. M. Albrecht, M. H. Madsen, E. Johnson, J. Nygård, C. M. Marcus, and

T. S. Jespersen, Epitaxy of semiconductor– superconductor nanowires, Nat. Mater. **14**, 400 (2015).

[18] W. Chang, S. M. Albrecht, T. S. Jespersen, F. Kuemmeth, P. Krogstrup, J. Nygård, and C. M. Marcus, Hard gap in epitaxial semiconductor– superconductor nanowires, Nat. Nanotechnol. **10**, 232 (2015).

[19] M. Kjaergaard, F. Nichele, H. J. Suominen, M. P. Nowak, M. Wimmer, A. R. Akhmerov, J. A. Folk, K. Flensberg, J. Shabani, C. J. Palmstrom, and C. M. Marcus, Quantized conductance doubling and hard gap in a two-dimensional semiconductor-superconductor heterostructure, Nat. Commun. **7**, 12841 (2016).

[20] J. Shabani, M. Kjaergaard, H. J. Suominen, Y. Kim, F. Nichele, K. Pakrouski, T. Stankevic, R. M. Lutchyn, P. Krogstrup, R. Feidenhans'l, S. Kraemer, C. Nayak, M. Troyer, C. M. Marcus, and C. J. Palmstrøm, Two-dimensional epitaxial superconductor-semiconductor heterostructures: A platform for topological superconducting networks, Phys. Rev. B **93**, 155402 (2016).

[21] A. C. C. Drachmann, H. J. Suominen, M. Kjaergaard, B. Shojaei, C. J. Palmstrøm, C. M. Marcus, and F. Nichele, Proximity effect transfer from NbTi into a semiconductor heterostructure via epitaxial aluminum, Nano Lett. **17**, 1200 (2017).

[22] M. Kjaergaard, H. J. Suominen, M. P. Nowak, A. R. Akhmerov, J. Shabani, C. J. Palmstrøm, F. Nichele, and C. M. Marcus, Transparent Semiconductor-Superconductor Interface and Induced Gap in an Epitaxial Heterostructure Josephson Junction, Phys. Rev. Appl. **7**, 034029 (2017).

[23] H. J. Suominen, M. Kjaergaard, A. R. Hamilton, J. Shabani, C. J. Palmstrøm, C. M. Marcus, and F. Nichele, Zero-Energy Modes from Coalescing Andreev States in a Two-Dimensional Semiconductor-Superconductor Hybrid Platform, Phys. Rev. Lett. **119**, 176805 (2017).

[24] L. Casparis, M. R. Connolly, M. Kjaergaard, N. J. Pearson, A. Kringhøj, T. W. Larsen, F. Kuemmeth, T. Wang, C. Thomas, S. Gronin, G. C. Gardner, M. J. Manfra, C. M. Marcus, and K. D. Petersson, Superconducting gatemon qubit based on a proximitized two-dimensional electron gas, Nat. Nanotechnol. **13**, 915 (2018).

[25] C. G. L. Bøttcher, F. Nichele, M. Kjaergaard, H. J. Suominen, J. Shabani, C. J. Palmstrøm, and C. M. Marcus, Superconducting, insulating and anomalous metallic regimes in a gated two-dimensional semiconductor– superconductor array, Nat. Phys. **14**, 1138 (2018).

[26] E. C. T. O'Farrell, A. C. C. Drachmann, M. Hell, A. Fornieri, A. M. Whiticar, E. B. Hansen, S. Gronin, G. C. Gardner, C. Thomas, M. J. Manfra, K. Flensberg, C. M. Marcus, and F. Nichele, Hybridization of Subgap States in One-Dimensional Superconductor-Semiconductor Coulomb Islands, Phys. Rev. Lett. **121**, 256803 (2018).

[27] J. S. Lee, B. Shojaei, M. Pendharkar, A. P. McFadden, Y. Kim, H. J. Suominen, M. Kjaergaard, F. Nichele, H. Zhang, C. M. Marcus, and C. J. Palmstrøm, Transport studies of Epi-Al/InAs two-dimensional electron gas systems for required building-blocks in topological superconductor networks, Nano Lett. **19**, 3083 (2019).

[28] W. Mayer, J. Yuan, K. S. Wickramasinghe, T. Nguyen, M. C. Dartiailh, and J. Shabani, Superconducting proximity effect in epitaxial Al-InAs heterostructures, Appl. Phys. Lett. **114**, 103104 (2019).

[29] A. C. C. Drachmann, R. E. Diaz, C. Thomas, H. J. Suominen, A. M. Whiticar, A. Fornieri, S. Gronin, T. Wang, G. C. Gardner, A. R. Hamilton, F. Nichele, M. J. Manfra, and C. M. Marcus, Anodic oxidation of epitaxial superconductor-semiconductor hybrids, Phys. Rev. Mater. **5**, 013805 (2021).

[30] F. Nichele, E. Portolés, A. Fornieri, A. M. Whiticar, A. C. C. Drachmann, S. Gronin, T. Wang, G. C. Gardner, C. Thomas, A. T. Hatke, M. J. Manfra, and C. M. Marcus, Relating Andreev Bound States and Supercurrents in Hybrid Josephson Junctions, Phys. Rev. Lett. **124**, 226801 (2020).

[31] A. M. Whiticar, A. Fornieri, E. C. T. O'Farrell, A. C. C. Drachmann, T. Wang, C. Thomas, S. Gronin, R. Kallaher, G. C. Gardner, M. J. Manfra, C. M. Marcus, and F. Nichele, Coherent transport through a Majorana island in an Aharonov–Bohm interferometer, Nat. Commun. **11**, 3212 (2020).

[32] D. Z. Haxell, M. Coraiola, D. Sabonis, M. Hinderling, S. C. ten Kate, E. Cheah, F. Krizek, R. Schott, W. Wegscheider, W. Belzig, J. C. Cuevas, and F. Nichele, Microwave-induced conductance replicas in hybrid Josephson junctions without Floquet-Andreev states, arXiv:2212.03554 [cond-mat].

[33] D. Z. Haxell, E. Cheah, F. Křížek, R. Schott, M. F. Ritter, M. Hinderling, W. Belzig, C. Bruder, W. Wegscheider, H. Riel, and F. Nichele, Measurements of Phase Dynamics in Planar Josephson Junctions and SQUIDs, Phys. Rev. Lett. **130**, 087002 (2023).

[34] A. Banerjee, M. Geier, M. A. Rahman, D. S. Sanchez, C. Thomas, T. Wang, M. J. Manfra, K. Flensberg, and C. M. Marcus, Control of Andreev Bound States using Superconducting Phase Texture, Phys. Rev. Lett. **130**, 116203 (2023).

[35] N. A. Güsken, T. Rieger, B. Bennemann, E. Neumann, M. I. Lepsa, T. Schäpers, and D. Grützmacher, MBE growth of Al/InAs and Nb/InAs superconducting hybrid nanowire structures, Nanoscale **9**, 16735 (2017).

[36] D. J. Carrad, M. Bjergfelt, T. Kanne, M. Aagesen, F. Krizek, E. M. Fiordaliso, E. Johnson, J. Nygård, and T. S. Jespersen, Shadow epitaxy for in situ growth of generic semiconductor/superconductor hybrids, Adv. Mater. **32**, 1908411 (2020).

[37] T. Kanne, M. Marnauza, D. Olsteins, D. J. Carrad, J. E. Sestoft, J. de Bruijckere, L. Zeng, E. Johnson, E. Olsson, K. Grove-Rasmussen, and J. Nygård, Epitaxial Pb on InAs nanowires for quantum devices, Nat. Nanotechnol. **16**, 776 (2021).

[38] M. Pendharkar, B. Zhang, H. Wu, A. Zarassi, P. Zhang, C. P. Dempsey, J. S. Lee, S. D. Harrington, G. Badawy, S. Gazibegovic, R. L. M. Op het Veld, M. Rossi, J. Jung, A.-H. Chen, M. A. Verheijen, M. Hocevar, E. P. A. M. Bakkers, C. J. Palmstrøm, and S. M. Frolov, Parity-preserving and magnetic field– resilient superconductivity in InSb nanowires with Sn shells, Science **372**, 508 (2021).

[39] P. Dang, G. Khalsa, C. S. Chang, D. S. Katzer, N. Nepal, B. P. Downey, V. D. Wheeler, A. Suslov, A. Xie, E. Beam, Y. Cao, C. Lee, D. A. Muller, H. G. Xing, D. J. Meyer, and D. Jena, An all-epitaxial nitride heterostructure with concurrent quantum Hall effect and superconductivity, Sci. Adv. **7**, eabf1388 (2021).

[40] P. Perla, H. A. Fonseka, P. Zellekens, R. Deacon, Y. Han, J. Kölzer, T. Mörstedt, B. Bennemann, A. Espiari, K. Ishibashi, D. Grützmacher, A. M. Sanchez, M. I. Lepsa, and T. Schäpers, Fully *in situ* Nb/InAs-nanowire Josephson junctions

by selective-area growth and shadow evaporation, Nanoscale Advances **3**, 1413 (2021).

[41] B. Kousar, D. J. Carrad, L. Stampfer, P. Krogstrup, J. Nygård, and T. S. Jespersen, InAs/MoRe hybrid semiconductor/superconductor nanowire devices, Nano Lett. **22**, 8845 (2022).

[42] S. A. Khan, C. Lampadaris, A. Cui, L. Stampfer, Y. Liu, S. J. Pauka, M. E. Cachaza, E. M. Fiordaliso, J.-H. Kang, S. Korneychuk, T. Mutas, J. E. Sestoft, F. Krizek, R. Tanta, M. C. Cassidy, T. S. Jespersen, and P. Krogstrup, Highly transparent gatable superconducting shadow junctions, ACS Nano **14**, 14605 (2020).

[43] M. S. Bjergfelt, D. J. Carrad, T. Kanne, E. Johnson, E. M. Fiordaliso, T. S. Jespersen, and J. Nygård, Superconductivity and parity preservation in As-Grown in islands on InAs nanowires, Nano Lett. **21**, 9875 (2021).

[44] M. Bjergfelt, D. J. Carrad, T. Kanne, M. Aagesen, E. M. Fiordaliso, E. Johnson, B. Shojaei, C. J. Palmstrøm, P. Krogstrup, T. S. Jespersen, and J. Nygård, Superconducting vanadium/indium-arsenide hybrid nanowires, Nanotechnology **30**, 294005 (2019).

[45] L. Jelver, P. M. Larsen, D. Stradi, K. Stokbro, and K. W. Jacobsen, Determination of low-strain interfaces via geometric matching, Phys. Rev. B **96**, 085306 (2017).

[46] C. Buzea and K. Robbie, Assembling the puzzle of superconducting elements: A review, Supercond. Sci. Technol. **18**, R1 (2005).

[47] B. van Heck, A. R. Akhmerov, F. Hassler, M. Burrello, and C. W. J. Beenakker, Coulomb-assisted braiding of Majorana fermions in a Josephson junction array, New J. Phys. **14**, 035019 (2012).

[48] T. E. O'Brien, P. Rożek, and A. R. Akhmerov, Majorana-Based Fermionic Quantum Computation, Phys. Rev. Lett. **120**, 220504 (2018).

[49] V. Fatemi, A. R. Akhmerov, and L. Bretheau, Weyl Josephson circuits, Phys. Rev. Res. **3**, 013288 (2021).

[50] R. M. Lutchyn, E. P. A. M. Bakkers, L. P. Kouwenhoven, P. Krogstrup, C. M. Marcus, and Y. Oreg, Majorana zero modes in superconductor– semiconductor heterostructures, Nat. Rev. Mater. **3**, 52 (2018).

[51] E. Külah, C. Reichl, J. Scharnetzky, L. Alt, W. Dietsche, and W. Wegscheider, The improved inverted AlGaAs/GaAs interface: Its relevance for high-mobility quantum wells and hybrid systems, Semicond. Sci. Technol. **36**, 085013 (2021).

[52] Z. Lei, E. Cheah, K. Rubi, M. E. Bal, C. Adam, R. Schott, U. Zeitler, W. Wegscheider, T. Ihn, and K. Ensslin, High-quality two-dimensional electron gas in undoped InSb quantum wells, Phys. Rev. Res. **4**, 013039 (2022).

[53] G. Myburg, F. Auret, W. Meyer, C. Louw, and M. van Staden, Summary of Schottky barrier height data on epitaxially grown n- and p-GaAs, Thin Solid Films **325**, 181 (1998).

[54] G. E. Blonder, M. Tinkham, and T. M. Klapwijk, Transition from metallic to tunneling regimes in superconducting microconstrictions: Excess current, charge imbalance, and supercurrent conversion, Phys. Rev. B **25**, 4515 (1982).

[55] R. Taboryski, T. Clausen, J. B. Hansen, J. L. Skov, J. Kutchinsky, C. B. So/rensen, and P. E. Lindelof, Andreev reflections at interfaces between Δ-doped GaAs and superconducting Al films, Appl. Phys. Lett. **69**, 656 (1996).

[56] J. Kutchinsky, R. Taboryski, T. Clausen, C. B. Sørensen, A. Kristensen, P. E. Lindelof, J. Bindslev Hansen, C. Schelde Jacobsen, and J. L. Skov, Decay Lengths for Diffusive Transport Activated by Andreev Reflections in Al/n-GaAs/Al Superconductor-Semiconductor-Superconductor Junctions, Phys. Rev. Lett. **78**, 931 (1997).

[57] C. Weeks, G. Rosenberg, B. Seradjeh, and M. Franz, Anyons in a weakly interacting system, Nat. Phys. **3**, 796 (2007).

[58] G. Rosenberg, B. Seradjeh, C. Weeks, and M. Franz, Creation and manipulation of anyons in a layered superconductor– two-dimensional electron gas system, Phys. Rev. B **79**, 205102 (2009).

[59] B. Zocher and B. Rosenow, Topological superconductivity in quantum Hall– superconductor hybrid systems, Phys. Rev. B **93**, 214504 (2016).

[60] T. Okugawa, S. Park, P. Recher, and D. M. Kennes, Vortex control in superconducting Corbino geometry networks, Phys. Rev. B **106**, 024501 (2022).

[61] A. Geim(Heym), V. Falko, S. Dubonos, and I. Grigorieva, Single magnetic flux tube in a mesoscopic two-dimensional electron gas conductor, Solid State Commun. **82**, 831 (1992).

[62] T. Tschirky, MBE Growth of 6.1A Family Semiconductor Heterostructures, Ph.D. thesis, ETH Zürich, Zürich, 2017.

[63] Z. Lei, C. A. Lehner, E. Cheah, M. Karalic, C. Mittag, L. Alt, J. Scharnetzky, W. Wegscheider, T. Ihn, and K. Ensslin, Quantum transport in high-quality shallow InSb quantum wells, Appl. Phys. Lett. **115**, 012101 (2019).

[64] M. Berl, L. Tiemann, W. Dietsche, H. Karl, and W. Wegscheider, Structured back gates for high-mobility two-dimensional electron systems using oxygen ion implantation, Appl. Phys. Lett. **108**, 132102 (2016).

[65] J. M. Meyer, J. Scharnetzky, M. Berl, W. Wegscheider, M. Hauser, W. Dietsche, K.-C. Wang, G. Klimeck, L. Tiemann, and R. H. Blick, Microwave-induced capacitance resonances and anomalous magnetoresistance in double quantum wells, J. Appl. Phys. **125**, 235707 (2019).

[66] M. P. Röösli, L. Brem, B. Kratochwil, G. Nicolí, B. A. Braem, S. Hennel, P. Märki, M. Berl, C. Reichl, W. Wegscheider, K. Ensslin, T. Ihn, and B. Rosenow, Observation of quantum Hall interferometer phase jumps due to a change in the number of bulk quasiparticles, Phys. Rev. B **101**, 125302 (2020).

[67] J. Scharnetzky, P. Baumann, C. Reichl, H. Karl, W. Dietsche, and W. Wegscheider, Donor implanted back-gates in GaAs for MBE-grown highest mobility two-dimensional electron systems, Semicond. Sci. Technol. **36**, 085012 (2021).

[68] M. Karalic, C. Mittag, S. Mueller, T. Tschirky, W. Wegscheider, K. Ensslin, T. Ihn, and L. Glazman, Phase slips and parity jumps in quantum oscillations of inverted InAs/GaSb quantum wells, Phys. Rev. B **99**, 201402(R) (2019).

[69] K. Shibata, M. Karalic, C. Mittag, T. Tschirky, C. Reichl, H. Ito, K. Hashimoto, T. Tomimatsu, Y. Hirayama, W. Wegscheider, T. Ihn, and K. Ensslin, Electric-field-induced two-dimensional hole gas in undoped GaSb quantum wells, Appl. Phys. Lett. **114**, 232102 (2019).

[70] K. Shibata, M. Karalic, C. Mittag, T. Tschirky, C. Reichl, H. Ito, K. Hashimoto, T. Tomimatsu, Y. Hirayama, W. Wegscheider, T. Ihn, and K. Ensslin, Magnetotransport of electrically induced two-dimensional hole gases in undoped GaSb quantum wells, Phys. Rev. Res. **2**, 033383 (2020).

[71] Z. Lei, C. A. Lehner, K. Rubi, E. Cheah, M. Karalic, C. Mittag, L. Alt, J. Scharnetzky, P. Märki, U. Zeitler, W. Wegscheider, T. Ihn, and K. Ensslin, Electronic g factor and magneto-transport in InSb quantum wells, Phys. Rev. Res. **2**, 033213 (2020).

[72] C. C. Koch, J. O. Scarbrough, and D. M. Kroeger, Effects of interstitial oxygen on the superconductivity of niobium, Phys. Rev. B **9**, 888 (1974).

[73] See Supplemental Material at http://link.aps.org/supplemental/10.1103/PhysRevMaterials.7.076201 for a more detailed discussion of (a) the vacuum and gas supply system of the UHV DC magnetron sputtering chamber, (b) the elemental analysis of the deposited Nb films, (c) the electrical measurement of the superconducting properties of the Nb films, and (d) extraction of the interlayer thicknesses from TEM images. The Supplemental Material additionally contains Refs. [116–121].

[74] C. J. Palmstrom, Epitaxy of dissimilar materials, Annu. Rev. Mater. Sci. **25**, 389 (1995).

[75] T. Sands, C. Palmstrøm, J. Harbison, V. Keramidas, N. Tabatabaie, T. Cheeks, R. Ramesh, and Y. Silberberg, Stable and epitaxial metal/III-V semiconductor heterostructures, Mater. Sci. Rep. **5**, 99 (1990).

[76] L. J. Brillson, *Surfaces and Interfaces of Electronic Materials* (Wiley-VCH, Weinheim, 2010).

[77] C. B. Alcock, V. P. Itkin, and M. K. Horrigan, Vapour pressure equations for the metallic elements: 298–2500K, Can. Metall. Q. **23**, 309 (1984).

[78] D. M. Mattox, *Handbook of Physical Vapor Deposition (PVD) Processing*, 2nd ed. (William Andrew, Oxford, UK, 2010).

[79] R. Mičunek, A. Plecenik, P. Kúš, M. Zahoran, M. Tomášek, T. Plecenik, M. Gregor, M. Štefečka, V. Jacko, J. Greguš, B. Grančič, M. Kubinec, and M. Mahel', Preparation of MgB_2 superconducting thin films by magnetron sputtering, Phys. C: Supercond. Appl. **435**, 78 (2006).

[80] O. V. Dobrovolskiy and M. Huth, Crossover from dirty to clean superconducting limit in dc magnetron-sputtered thin Nb films, Thin Solid Films **520**, 5985 (2012).

[81] T. Imamura, T. Shiota, and S. Hasuo, Fabrication of high quality Nb/AlO/sub x/-Al/Nb Josephson junctions. I. Sputtered Nb films for junction electrodes, IEEE Trans. Appl. Supercond. **2**, 1 (1992).

[82] D. Nečas and P. Klapetek, Gwyddion: An open-source software for SPM data analysis, Open Phys. **10**, 181 (2012).

[83] T. de Freitas, J. Gonzalez, V. Nascimento, and E. Passamani, The role of the substrate temperature on superconducting properties of sputtered Nb films, Thin Solid Films **611**, 33 (2016).

[84] S. Wilde, R. Valizadeh, O. B. Malyshev, G. B. G. Stenning, T. Sian, and B. Chesca, Dc magnetometry of niobium thin film superconductors deposited using high power impulse magnetron sputtering, Phys. Rev. Accel. Beams **21**, 073101 (2018).

[85] J. M. Monti, J. A. Stewart, J. O. Custer, D. P. Adams, D. Depla, and R. Dingreville, Linking simulated polycrystalline thin film microstructures to physical vapor deposition conditions, Acta Mater. **245**, 118581 (2023).

[86] H. R. Kerchner, D. K. Christen, and S. T. Sekula, Critical fields H_c and H_{c2} of superconducting niobium, Phys. Rev. B **24**, 1200 (1981).

[87] M. Tinkham, *Introduction to Superconductivity*, 2nd ed., International Series in Pure and Applied Physics (McGraw Hill, New York, 1996).

[88] Th. Schäpers, V. A. Guzenko, R. P. Müller, A. A. Golubov, A. Brinkman, G. Crecilius, A. Kaluza, and H. Lüth, Current-injection in a ballistic multiterminal superconductor/two-dimensional electron gas Josephson junction, Phys. Rev. B **67**, 014522 (2003).

[89] C. Peroz and C. Villard, Flux flow properties of niobium thin films in clean and dirty superconducting limits, Phys. Rev. B **72**, 014515 (2005).

[90] I. Zaytseva, O. Abal'oshev, P. Dłużewski, W. Paszkowicz, L. Y. Zhu, C. L. Chien, M. Kończykowski, and M. Z. Cieplak, Negative Hall coefficient of ultrathin niobium in Si/Nb/Si tri-layers, Phys. Rev. B **90**, 060505(R) (2014).

[91] J. H. Quateman, T_c suppression and critical fields in thin superconducting Nb films, Phys. Rev. B **34**, 1948 (1986).

[92] M. S. M. Minhaj, S. Meepagala, J. T. Chen, and L. E. Wenger, Thickness dependence on the superconducting properties of thin Nb films, Phys. Rev. B **49**, 15235 (1994).

[93] I. Zaytseva, A. Abaloszew, B. C. Camargo, Y. Syryanyy, and M. Z. Cieplak, Upper critical field and superconductor-metal transition in ultrathin niobium films, Sci. Rep. **10**, 19062 (2020).

[94] N. W. Ashcroft and N. D. Mermin, *Solid State Physics* (Holt, Rinehart and Winston, New York, 1976).

[95] A. I. Gubin, K. S. Il'in, S. A. Vitusevich, M. Siegel, and N. Klein, Dependence of magnetic penetration depth on the thickness of superconducting Nb thin films, Phys. Rev. B **72**, 064503 (2005).

[96] D. Hazra, M. Mondal, and A. K. Gupta, Correlation between structural and superconducting properties of nano-granular disordered Nb thin films, Phys. C: Supercond. **469**, 268 (2009).

[97] A. F. Mayadas, R. B. Laibowitz, and J. J. Cuomo, Electrical characteristics of rf-sputtered single-crystal niobium films, J. Appl. Phys. **43**, 1287 (1972).

[98] D. K. Schroder, *Semiconductor Material and Device Characterization*, 3rd ed. (IEEE Press; Wiley, Piscataway, NJ: Hoboken, NJ, 2006).

[99] A. Leo, G. Grimaldi, R. Citro, A. Nigro, S. Pace, and R. P. Huebener, Quasiparticle scattering time in niobium superconducting films, Phys. Rev. B **84**, 014536 (2011).

[100] N. Pinto, S. J. Rezvani, A. Perali, L. Flammia, M. V. Milošević, M. Fretto, C. Cassiago, and N. De Leo, Dimensional crossover and incipient quantum size effects in superconducting niobium nanofilms, Sci. Rep. **8**, 4710 (2018).

[101] N. R. Werthamer, E. Helfand, and P. C. Hohenberg, Temperature and purity dependence of the superconducting critical field, H_{c2}. III. Electron spin and spin-orbit effects, Phys. Rev. **147**, 295 (1966).

[102] K. Maki, Effect of pauli paramagnetism on magnetic properties of high-field superconductors, Phys. Rev. **148**, 362 (1966).

[103] A. Gurevich, Enhancement of the upper critical field by nonmagnetic impurities in dirty two-gap superconductors, Phys. Rev. B **67**, 184515 (2003).

[104] K. Ilin, D. Henrich, Y. Luck, Y. Liang, M. Siegel, and D. Yu. Vodolazov, Critical current of Nb, NbN, and TaN thin-film bridges with and without geometrical nonuniformities in a magnetic field, Phys. Rev. B **89**, 184511 (2014).

[105] R. F. Wang, S. P. Zhao, G. H. Chen, and Q. S. Yang, Absolute measurement of penetration depth in a superconducting film by the two-coil technique, Appl. Phys. Lett. **75**, 3865 (1999).

[106] K. Fuchs, The conductivity of thin metallic films according to the electron theory of metals, Math. Proc. Camb. Philos. Soc. **34**, 100 (1938).

[107] A. F. Mayadas and M. Shatzkes, Electrical-resistivity model for polycrystalline films: The case of arbitrary reflection at external surfaces, Phys. Rev. B **1**, 1382 (1970).

[108] J. Vancea, G. Reiss, and H. Hoffmann, Mean-free-path concept in polycrystalline metals, Phys. Rev. B **35**, 6435 (1987).

[109] P. Mangin and R. Kahn, *Superconductivity* (Springer Berlin Heidelberg, New York, NY, 2016).

[110] U. Welp, Z. L. Xiao, J. S. Jiang, V. K. Vlasko-Vlasov, S. D. Bader, G. W. Crabtree, J. Liang, H. Chik, and J. M. Xu, Superconducting transition and vortex pinning in Nb films patterned with nanoscale hole arrays, Phys. Rev. B **66**, 212507 (2002).

[111] U. Welp, X. L. Xiao, V. Novosad, and V. K. Vlasko-Vlasov, Commensurability and strong vortex pinning in nanopatterned Nb films, Phys. Rev. B **71**, 014505 (2005).

[112] A. G. Baca and C. I. H. Ashby, *Fabrication of GaAs Devices*, Processing Series No. no. 6 (Institution of Electrical Engineers, London, UK, 2005).

[113] J. Ding, B. Lee, R. Gronsky, J. Washburn, D. Chin, and T. Van Duzer, High-temperature stability of Nb/GaAs and NbN/GaAs interfaces, Appl. Phys. Lett. **52**, 135 (1988).

[114] J. Kutchinsky, R. J. Taboryski, T. Clausen, C. B. Sørensen, P. E. Lindelof, J. B. Hansen, C. S. Jacobsen, and J. L. Skov, Diffusive electronic transport in superconductor-semiconductor-superconductor junctions of Al or Nb on δ-doped GaAs, Czech. J. Phys. **46**, 671 (1996).

[115] F. Giazotto, P. Pingue, F. Beltram, M. Lazzarino, D. Orani, S. Rubini, and A. Franciosi, Resonant Transport in Nb / GaAs / AlGaAs Heterostructures: Realization of the de Gennes–Saint-James Model, Phys. Rev. Lett. **87**, 216808 (2001).

[116] P. Fulde and K. Maki, Theory of superconductors containing magnetic impurities, Phys. Rev. **141**, 275 (1966).

[117] T. R. Lemberger and D. M. Ginsberg, Measurement of the upper critical magnetic field of superconductors with magnetic impurities, Phys. Rev. B **18**, 6105 (1978).

[118] A. Chevarier, N. Chevarier, M. El Bouanani, E. Gerlic, M. Stern, B. Roux, and F. Thimon, Profiling of carbon, oxygen and argon contamination in sputter-deposited films using nuclear backscattering and nuclear reaction spectroscopy, Appl. Surf. Sci. **48–49**, 215 (1991).

[119] C. Henriot, P. Bosland, B. Coadou, J. Rodriguez, and J. Leclerc, Niobium getter effect, Vacuum **43**, 651 (1992).

[120] N. Iosad, T. Klapwijk, S. Polyakov, V. Roddatis, E. Kov'ev, and P. Dmitriev, Properties of DC magnetron sputtered Nb and NbN films for different source conditions, IEEE Trans. Appl. Supercond. **9**, 1720 (1999).

[121] M. David Henry, S. Wolfley, T. Monson, B. G. Clark, E. Shaner, and R. Jarecki, Stress dependent oxidation of sputtered niobium and effects on superconductivity, J. Appl. Phys. **115**, 083903 (2014).